

Harvesting, coupling and control of single exciton coherences in photonic waveguide antennas

Q. Mermillod,^{1,2,*} T. Jakubczyk,^{1,2} V. Delmonte,^{1,2} A. Delga,^{1,3}
E. Peinke,^{1,3} J-M. Gérard,^{1,3} J. Claudon,^{1,3} and J. Kasprzak^{1,2,†}

¹*Univ. Grenoble Alpes, F-38000 Grenoble, France*

²*CNRS, Institut Néel, "Nanophysique et semiconducteurs" group, F-38000 Grenoble, France*

³*CEA, INAC-PHELIQS, "Nanophysique et semiconducteurs" group, F-38000 Grenoble, France*

We perform coherent non-linear spectroscopy of individual excitons strongly confined in single InAs quantum dots (QDs). The retrieval of their intrinsically weak four-wave mixing (FWM) response is enabled by a one-dimensional dielectric waveguide antenna. Compared to a similar QD embedded in bulk media, the FWM detection sensitivity is enhanced by up to four orders of magnitude, over a broad operation bandwidth. Three-beam FWM is employed to investigate coherence and population dynamics within individual QD transitions. We retrieve their homogenous dephasing in a presence of spectral wandering. Two-dimensional FWM reveals off-resonant Förster coupling between a pair of distinct QDs embedded in the antenna. We also detect a higher order QD non-linearity (six-wave mixing) and use it to coherently control the FWM transient. Waveguide antennas enable to conceive multi-color coherent manipulation schemes of individual emitters.

Semiconductor quantum dots (QDs) embedded in properly designed photonic nanostructures hold great promises for future quantum information technologies¹. These few-level mesoscopic emitters can serve as bright sources of non-classical states of light²⁻⁴ or mediate strong optical non-linearities, at the single-photon level^{5,6}. An excitonic QD transition also constitutes a localized qubit that can be coherently manipulated on sub-ps timescale with optical pulses⁷⁻⁹. Via coupling QD excitons with solid-state spins, one can combine fast radiative emission with a long-lived spin coherence. A spin-photon interface, a prerequisite for a distributed quantum network, has been recently demonstrated with such systems¹⁰. In this dynamic context, an accurate assessment and control of the excitonic coherence is required. Furthermore, harnessing inter-exciton coupling mechanisms is of utmost importance for implementing non-local coherent control schemes.

Coherent non-linear spectroscopy provides avant-garde techniques for all-optical coherent manipulation and readout of single emitters⁹, in particular by investigating four-wave mixing (FWM). As depicted in Fig. 2, such polarization is driven by three, resonant, short laser pulses with electric field amplitudes \mathcal{E}_1 , \mathcal{E}_2 and \mathcal{E}_3 . In the lowest order, FWM is proportional to $\mu^4 \mathcal{E}_1^* \mathcal{E}_2 \mathcal{E}_3$, with μ denoting the optical dipole moment of the emitter. By taking advantage of the photon echo formation¹¹, FWM has been exploited in the past to infer spectral homogenous broadening in ensembles of optical transitions in solids, even in a presence of inhomogeneous broadening. Due to the steep dependence on μ , first investigations of FWM on *single* emitters have been limited to giant oscillator strength excitons confined by interface fluctuations of a quantum well^{12,13}. A successful strategy to improve the FWM retrieval relies on photonic structures that locally enhance the driving fields experienced by the QD and improve the collection efficiency of the generated nonlinear response. In particular, semiconductor micro-cavities have shown appealing prospects^{5,9,14}, albeit at the cost of an operation bandwidth limited to the cavity resonance.

In this Letter, we show that waveguide antennas, initially introduced to realize bright sources of quantum light^{2,15}, dramatically enhance the non-linear response of individual QDs over a broad spectral range. This enhancement enables a comprehensive investigation of the coherence properties of excitonic complexes strongly confined in self-assembled InAs QDs. While such emitters constitute one of the leading systems for solid-state quantum optics^{1,4}, their moderate oscillator strength has hindered investigations of coherence at the single QD level. Furthermore, we show that FWM can reveal an off-resonant coherent coupling via underlying Coulomb interaction between two distinct QDs embedded in the antenna. Finally, we recover six-wave mixing (SWM) of an exciton-biexciton system, and use it to coherently control the FWM transient. Our findings pave the way towards achieving non-local, coherent control in small sets of individual emitters in a solid.

The antenna, shown in Fig. 1 a, is a suspended GaAs photonic trumpet¹⁵ (PT), which is anchored to square pillars for improved mechanical stability. The driving pulses $\mathcal{E}_{1,2,3}$ are focused on the circular top facet. Thanks to the nearly Gaussian profile of the fundamental guided mode (HE_{11})¹⁶, Gaussian driving beams with adapted waists are transmitted to the tapered section with negligible losses. On the waveguide axis, the electrical field amplitude scales as $\sqrt{n_g/S_{\text{eff}}}$, with n_g the group index and S_{eff} the effective mode surface¹⁷. Field enhancement reaches a maximum at the QDs position, when the waveguide diameter is reduced down to $0.25 \mu\text{m}$, mainly because of the optimal lateral confinement of the mode, assisted by a modest slow-light effect¹⁷. Compared to a QD embedded in bulk GaAs, a factor of ~ 100 is gained on the global amplitude $\mathcal{E}_1 \mathcal{E}_2 \mathcal{E}_3$, which drives the FWM. Conversely, the collection efficiency of the generated FWM increases from around 1% up to 45%. As a consequence, the FWM is retrieved with signal-to-background ratio improved by a factor of $\sim 4 \times 10^3$. Moreover, these non-resonant photonic structures naturally provide a large operation bandwidth ($> 100 \text{ nm}$)¹⁸.

The wave-mixing signals are retrieved by hetero-

dyne spectral interferometry technique¹². Employing acousto-optic modulation, the driving pulses $\mathcal{E}_{1,2,3}$ are frequency up-shifted by radio-frequencies $\Omega_{1,2,3}$ introducing controlled phase-drifts in their respective trains. After having acquired delays τ_{12} and τ_{23} , $\mathcal{E}_{1,2,3}$ are recombined into a common spatial mode and are focused on the sample with a microscope objective. An unmodulated reference beam is focused on the auxiliary pillar (see Fig. 1 a) and the searched response is discriminated in the reflectance by the phase-sensitive optical heterodyning, attaining a selectivity in field (intensity) of 10^6 (10^{12}). The experimental setup is described in Ref. [9]. Measurements are conducted on a structure similar to the one shown in Fig. 1 a, maintained at $T = 5.2 \pm 0.5$ K.

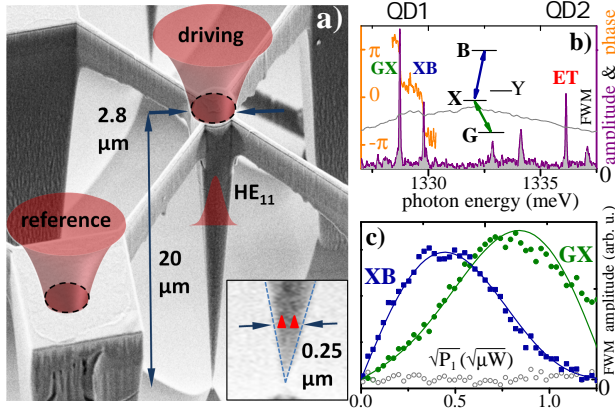


FIG. 1. **Nanowire antenna for enhancing the four-wave mixing (FWM) response of excitonic transitions strongly confined in InAs QDs.** a) SEM image of a suspended photonic trumpet, which is made of GaAs and embeds a few self-assembled InAs QDs close to its base (inset). This photonic structure simultaneously improves the in-coupling of the resonant driving pulses to the QDs and the out-coupling of the non-linear signal to the collection optics. Also see section A in the SM. b) Spectrally-resolved FWM amplitude (violet) and phase (orange). The pulse sequence of Fig. 2 a is employed, with $\tau_{12} = 10$ ps, $(\theta_1, \theta_2) = (\pi/5, 2\pi/5)$. The excitation spectrum is given with a gray line. c) FWM amplitude as a function of \mathcal{E}_1 pulse area $\theta_1 \propto \sqrt{P_1}$, showing Rabi oscillation at GX (green circles) and XB (blue squares) transitions. The open symbols give the noise floor. The theoretical predictions appear as solid lines. Measurement parameters: $\theta_2 = 0.82\pi$, $\tau_{12} = 5$ ps.

To explore the coherence dynamics of QD excitons, we first concentrate on degenerate FWM. It is generated by a two-pulse sequence, as depicted in Fig. 2 a and retrieved at the $2\Omega_2 - \Omega_1$ heterodyne frequency. The spectrally-resolved FWM amplitude and phase are shown in Fig. 1 b. The sharp peaks correspond to individual excitonic transitions. Having verified the FWM polarization selection rules, the resonances GX and XB are unequivocally recognized as ground state-exciton and exciton-biexciton transitions, hosted by a first QD, labeled QD1 [see section C of the Supplementary Material (SM)]. Note the negative biexciton renormalization energy of $\Delta \simeq -1$ meV, indicating a small spatial extent of wavefunctions of the both complexes and thus their small μ . Such sys-

tem is a generic excitation in neutral QDs, in particular enabling bright generation of entangled photon pairs from solid state devices¹⁹. ET, which will be discussed latter, is attributed to a charged exciton (trion), hosted by a different QD, labeled QD2.

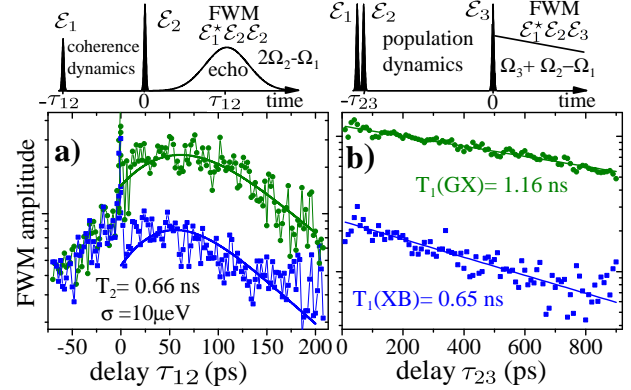


FIG. 2. **Coherence and population dynamics in the exciton-biexciton system of QD1.** a) Coherence dynamics is investigated via degenerate FWM. The top panel indicates the pulse sequence and the related observable. The dependence of the FWM signal on τ_{12} yields T_2 and σ , for both GX and XB transitions. Applied pulse areas: $(\theta_1, \theta_2) = (\pi/5, 2\pi/5)$. b) Population dynamics is investigated via non-degenerate FWM (top panel). The dependence of the FWM signal on τ_{23} yields T_1 for X and B states. Measurement parameters: $\tau_{12} = 1$ ps, $(\theta_1, \theta_2, \theta_3) = (\pi/2, \pi/2, \pi/2)$. Both graphs feature logarithmic vertical scales.

To directly illustrate the enhanced in-coupling of the driving pulses, we present in Fig. 1 c FWM amplitudes of GX and XB as a function of \mathcal{E}_1 pulse area θ_1 (being proportional to the square-root of pulse \mathcal{E}_1 intensity P_1). The FWM of both transitions reaches its maximum, corresponding to the $\theta_1 = \pi/2$, for impressively low \mathcal{E}_1 intensity of around $0.3 \mu\text{W}$, two orders of magnitude less than in strongly-confined GaAs QDs²⁰ embedded in bulk. Further increase of θ_1 results in Rabi flopping modeled using analytical prediction²⁰ only by adjusting XB to GX dipole moment ratio $\mu_{XB}/\mu_{GX} = 0.9$ (see solid lines in Fig. 1 c).

As a first application of enhanced FWM harvesting, we conduct a comprehensive investigation of the coherence and population dynamics of individual excitonic transitions hosted by a QD, a task that is relevant for all applications of this system to quantum information technologies. Coherence dynamics is investigated by measuring FWM as a function of the pulse separation τ_{12} , as depicted in Fig. 2 a. Importantly, this technique allows to disentangle homogeneous and inhomogeneous dephasing processes. The former is due to radiative recombination and pure dephasing, while the latter is associated with spectral fluctuations of the transition energy²⁰. As a representative example, we consider in Fig. 2 a the transitions GX and XB hosted by QD1. The initial rise for $\tau_{12} > 0$, followed by an exponential decay, is due to the formation of a photon echo triggered by a spectral wandering, which acts as a source of inhomogeneous broadening (other examples are given in section B of

the SM). Using the model presented in Ref. [20], we obtain the dephasing time $T_2 = (0.66 \pm 0.05)$ ns, in agreement with measurements performed on ensembles²¹. In addition, the data reveal a Gaussian inhomogeneous broadening, characterized by a full-width at half maximum $\sigma = (10 \pm 4)$ μ eV. Also, it is worth to note the presence of the signal for $\tau_{12} < 0$, generated by a two-photon coherence in a four-level exciton-biexciton system²⁰. From the FWM decay at negative delays we estimate two-photon dephasing time of $T_{\text{TPC}} = (41 \pm 13)$ ps.

Population evolution is investigated with a three pulse sequence, shown in Fig. 2b. Here, \mathcal{E}_1 and \mathcal{E}_2 first create X and B population oscillating at $\Omega_2 - \Omega_1$. The last pulse, \mathcal{E}_3 , creates a polarization proportional to this density, the FWM, which is detected at the $\Omega_3 + \Omega_2 - \Omega_1$ frequency. Thus varying delay τ_{23} between \mathcal{E}_2 and \mathcal{E}_3 , the measured FWM reflects the population evolution in a QD. From the resulting exponential decays of the FWM amplitude we retrieve the exciton and biexciton lifetimes of $T_1(\text{GX}) = (1.16 \pm 0.04)$ ns and $T_1(\text{XB}) = (0.65 \pm 0.05)$ ns, respectively, with their ratio approaching theoretical limit²² of two.

These measurements show that the investigated transitions are not radiatively limited. For GX, T_2 is 3.5 times smaller than $2T_1$ and this factor is reduced to 2 for XB, which presents a faster population decay. In addition, a significant spectral wandering σ is present. Such high- and low-frequency noises are likely to be mainly caused by fluctuations of charge traps located close to the QD^{23,24}, either in its immediate environment or in the wire sidewall. While further research is necessary to elucidate this point, the application of a dc electric field on the QDs^{25,26} could help reducing σ , further improving the coherence retrieval.

Beyond assessment of the single-QD coherence, we show below that FWM can reveal a coherent^{13,14,27,28}, non-resonant coupling between QD1 and QD2. Establishing coherence transfer between a pair of emitters is an essential ingredient to achieve optically controlled two-qubit operations in solid. In a broader context, the coherence and charge transfer is a multidisciplinary issue, spanning from biology, where it is at heart of photosynthesis²⁹, towards quantum chemistry and photovoltaics. Here, we investigate FWM simultaneously driven at GX, XB (QD1) and ET (QD2). As shown in Fig. 3a, the coherence dynamics of XB is dominated by the exciton-biexciton beating with a period $|2\pi\hbar/\Delta| \simeq 4.5$ ps driven by fifth-order contributions to the FWM³⁰, predominant upon $(\theta_1, \theta_2) \simeq (\pi/2, \pi)$ employed here. Additionally, we observe a modulation with a period 0.58 ps, particularly pronounced on the ET transition and corresponding to the spectral separation between both QDs, hence indicating their mutual coupling.

Its definite display is provided by the two-dimensional FWM spectrum^{13,14} shown in Fig. 3b. By Fourier-transforming the FWM along the delay τ_{12} we obtain a map linking the first-order absorption frequency ω_1 , with the FWM one, ω . The off-diagonal signals in such a diagram are signatures of coherent

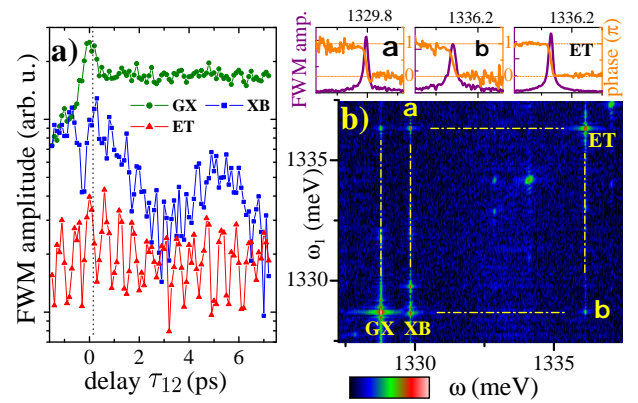


FIG. 3. Coherent, off-resonant coupling between QD1 and QD2. We investigate here degenerate FWM (pulse sequence shown in Fig. 2a) with a non-perturbative driving: $(\theta_1, \theta_2) = (\pi/2, \pi)$. a) Delay dependence of the FWM amplitude for GX, XB (QD1) and ET (QD2). b) Amplitude of the two-dimensional FWM: coherent coupling is evidenced by a pair of off-diagonal peaks, forming square features depicted with the dashed lines. Note the presence of the diagonal peak for XB induced by the non-perturbative driving. Logarithmic scale over two orders of magnitude, given by the bar. Top: FWM amplitude and phase of the off-diagonal peaks, labeled α and β at $\omega = (1329.8, 1336.16)$ meV and the diagonal ET peak.

coupling, i.e. conversion of the absorbed ω_1 into different ω , as depicted by squares. The mutual coupling within the triplet (GX, XB, ET) is thus detected. The internal coupling in QD1, i.e. between GX and XB, is expected^{13,20}. Conversely, the transfer of coherence toward ET in QD2 is more intriguing. Owing to a large frequency detuning between ET and GX, radiative coupling³¹ is excluded. Coherent coupling between excitons in closely lying QDs stems from their Coulomb interaction^{13,27,28}, inducing biexciton shift or/and dipole-dipole Förster coupling. To distinguish between both mechanisms, in Fig. 3b (top) we inspect the amplitude and phase of the off-diagonal terms in the 2D FWM¹³: the former generates a double-peak and 2π spectral shift across the off-diagonal signal, while the latter produces a single off-diagonal peak with a 1π phase shift. This last scenario is indeed revealed by the experimental data, indicating Förster coupling between QD1 and QD2. The spectral shift between the uncoupled and coupled states is not detected owing to the large spectral detuning of both QDs with respect to the dipole coupling strength estimated to a few hundred of μ eV. More involved multidimensional spectroscopy²⁸ could provide additional insights into the microscopic mechanism of the observed coupling. We note that the broad operation bandwidth of the PT is here instrumental to reveal such a largely off-resonant Förster coupling between QD1 and QD2.

In the following, we exploit a novel three-pulse sequence⁹ to demonstrate coherent control of the FWM generated by the exciton-biexciton system of QD1. The protocol is based on converting a desired amount of the FWM transient into the six-wave mixing (SWM) one. The applied pulse sequence is de-

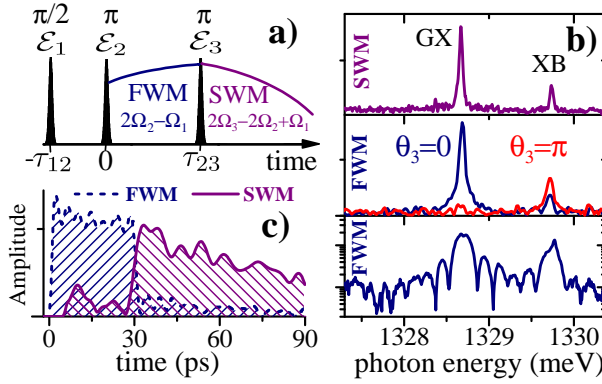


FIG. 4. **Three-pulse coherent control of the exciton-biexciton system in QD1.** a) A sketch of the pulse sequence and their areas employed to drive the SWM and to manipulate the FWM transient via FWM/SWM conversion scheme. b) Top: SWM spectrum of GX and XB: $(\tau_{12}, \tau_{23}) = (15, 30)$ ps, $(\theta_1, \theta_2, \theta_3) = (\pi/2, \pi, \pi)$. Middle: Coherent control of the GX and XB by FWM/SWM switching: $\theta_3 = 0$ and $\theta_3 = \pi$ correspond to blue and red spectra, respectively. Bottom: Manipulation of the FWM spectral response of the GX and XB: $\theta_3 = \pi$, $\tau_{23} = 30$ ps. c) Conversion of the FWM to SWM observed on the GX in time domain: $\theta_3 = \pi$, $\tau_{23} = 30$ ps.

picted in Fig. 4a. First, \mathcal{E}_1 and \mathcal{E}_2 drive degenerate FWM, which is evolving during τ_{23} . Then, \mathcal{E}_3 is used to flip it into the specific SWM frequency. The amount of FWM converted to SWM is governed by θ_3 . In particular, for $\theta_3 = \pi$ the entirety of FWM is transferred to SWM. Such control via FWM/SWM switching represents a step change with respect to past FWM experiments, as it enables to accurately design the FWM response in temporal and frequency domains, by tuning τ_{23} and θ_3 . The SWM spectrum of the investigated exciton-biexciton system driven at $(\theta_1, \theta_2, \theta_3) = (\pi/2, \pi, \pi)$ is shown in Fig. 4b (top). In the middle panel we present the corresponding FWM: for $\theta_3 = 0$ and $\tau_{12} = 3$ ps (dark blue) we recover the response as in Fig. 1b. Instead, for $\theta_3 = \pi$ (red) the FWM of the GX transition is quenched, whereas the one of XB is enhanced. Such a FWM/SWM switching at the GX transition is retrieved in the time domain in Fig. 4c. At the arrival of \mathcal{E}_3 for $\tau_{23} = 30$ ps the FWM is virtually suppressed, while the onset of the SWM is observed. An abrupt cut of the signal in time domain induces a particular FWM spectral line-shape⁹ of GX and XB, with a broadening of the main peaks and

build up of side-bands, exemplified in Fig. 4b (bottom) for $\tau_{23} = 30$ ps. This effect, along with the temporal gating of the FWM, is visualized in more details in the Supplementary Figure S8, displaying FWM spectra and transients when varying τ_{23} . Note that the presented control scheme necessitates addressing individual transitions in contrast to past SWM experiments^{30,32,33}. Demonstration of SWM beyond two-level system, paves the way towards three-dimensional spectroscopy (involving the interplay between absorption, FWM and SWM) of quantum emitters, opening new frontiers to monitor couplings and control the coherence in condensed matter. Furthermore, prospective SWM studies on individual QDs could elucidate their non-Markovian dephasing³³.

To conclude, we performed coherent nonlinear spectroscopy of single, strongly-confined excitons in InAs QDs embedded in PTs. Such waveguide antennas offer a perfect interfacing of QD excitons with external excitation, enabling to harvest their multi-wave mixing responses with a sensitivity improved by up to four-orders of magnitude with respect to a QD in bulk GaAs. Wave mixing spectroscopy was employed not only to assess the coherence of individual transitions, but also to ascertain inter-exciton couplings with 2D FWM and to manipulate coherent response via FWM/SWM switching. The broad operation bandwidth of the antenna opens new possibilities for coherent spectroscopy of single emitters, like performing multi-color multi-wave mixing. With such a prospective Raman-type spectroscopy on single QDs³⁴, one could for example explore dynamics of optical polarons^{35,36} (coupled exciton - optical phonon modes) and study propagation of acoustic phonons between off-resonant, spatially distant excitons. The broadband character of PTs also enables to perform wave-mixing spectroscopy on excited states of a QD, to determine its level structure and to retrieve related dephasings and coherent couplings. Finally, by exploiting the energy tunability via strain³⁷, a pair of separate excitons could be brought into the frequency resonance, so as to induce a radiative coupling³¹ mediated by the photons guided by the wire antenna.

We acknowledge the support by the ERC Starting Grant PICSEN, contract no. 306387. Sample fabrication was carried out in the “Plateforme Technologique Amount (PTA)” and CEA LETI MINATEC/DOPT clean rooms. JK thanks Wolfgang Langbein for fruitful discussions and continuous support.

* quentin.mermillod@neel.cnrs.fr

† jacek.kasprzak@neel.cnrs.fr

¹ Lodahl, P., Mahmoodian, S. & Stobbe, S. Interfacing single photons and single quantum dots with photonic nanostructures. *Rev. Mod. Phys.* **87**, 347 (2015).

² Claudon, J. *et al.* A highly efficient single-photon source based on a quantum dot in a photonic nanowire. *Nat. Photon.* **4**, 174 (2010).

³ Dousse, A. *et al.* A solid state ultrabright source of entangled photon pairs. *Nature* **466**, 217 (2011).

⁴ Schulte, C. H. H. *et al.* Quadrature squeezed photons

from a two-level system. *Nature* **525**, 222–225 (2015).

⁵ Kasprzak, J. *et al.* Up on the Jaynes-Cummings ladder of a quantum-dot/microcavity system. *Nat. Mater.* **9**, 304–308 (2010).

⁶ Javadi, A. *et al.* Single-photon non-linear optics with a quantum dot in a waveguide. *Nature Commun.* **6**, 8655 (2015).

⁷ Zrenner, A. *et al.* Coherent properties of a two-level system based on a quantum-dot photodiode. *Nature* **418**, 612 (2002).

⁸ Ramsay, A. J. *et al.* Phonon-induced rabi-

- frequency renormalization of optically driven single InGaAs/GaAs quantum dots. *Phys. Rev. Lett.* **105**, 177402 (2010).
- ⁹ Fras, F. *et al.* Multi-wave coherent control of a solid state single emitter. *Nat. Phot.* **10**, 155–158 (2016).
 - ¹⁰ Gao, W. B., Imamoglu, A., Bernien, H. & Hanson, R. Coherent manipulation, measurement and entanglement of individual solid-state spins using optical fields. *Nat. Photon.* **9**, 363 (2015).
 - ¹¹ Chemla, D. S. & Shah, J. Many-body and correlation effects in semiconductors. *Nature* **411**, 549–557 (2001).
 - ¹² Langbein, W. & Patton, B. Microscopic measurement of photon echo formation in groups of individual excitonic transitions. *Phys. Rev. Lett.* **95**, 017403 (2005).
 - ¹³ Kasprzak, J., Patton, B., Savona, V. & Langbein, W. Coherent coupling between distant excitons revealed by two-dimensional nonlinear hyperspectral imaging. *Nat. Phot.* **5**, 57–63 (2011).
 - ¹⁴ Albert, F. *et al.* Microcavity controlled coupling of excitonic qubits. *Nat. Comm.* **4**, 1747 (2013).
 - ¹⁵ Munsch, M. *et al.* Dielectric GaAs antenna ensuring an efficient broadband coupling between an InAs quantum dot and a Gaussian optical beam. *Phys. Rev. Lett.* **110**, 177402 (2013).
 - ¹⁶ Stepanov, P. *et al.* Highly directive and Gaussian far-field emission from “giant” photonic trumpets. *Appl. Phys. Lett.* **107**, 141106 (2015).
 - ¹⁷ Bleuse, J. *et al.* Inhibition, enhancement, and control of spontaneous emission in photonic nanowires. *Phys. Rev. Lett.* **106**, 103601 (2011).
 - ¹⁸ Claudon, J., Gregersen, N., Lalanne, P. & Gérard, J.-M. Harnessing light with photonic nanowires: fundamentals and applications to quantum optics. *Chem. Phys. Chem.* **14**, 2393–2402 (2013).
 - ¹⁹ Stevenson, R. M. *et al.* A semiconductor source of triggered entangled photon pairs. *Nature* **439**, 179 (2006).
 - ²⁰ Kasprzak, J. *et al.* Vectorial nonlinear coherent response of a strongly confined exciton-biexciton system. *New J. Phys.* **15**, 055006 (2013).
 - ²¹ Borri, P. *et al.* Exciton dephasing via phonon interactions in InAs quantum dots: Dependence on quantum confinement. *Phys. Rev. B* **71**, 115328 (2005).
 - ²² Bacher, G. *et al.* Biexciton versus exciton lifetime in a single semiconductor quantum dot. *Phys. Rev. Lett.* **83**, 4417 (1999).
 - ²³ Berthelot, A. *et al.* Unconventional motional narrowing in the optical spectrum of a semiconductor quantum dot. *Nat. Phys.* **2**, 759 (2006).
 - ²⁴ Kuhlmann, A. V. *et al.* Charge noise and spin noise in a semiconductor quantum device. *Nat. Phys.* **9**, 570 (2013).
 - ²⁵ Gregersen, N., Nielsen, T. R., Mørk, J., Claudon, J. & Gérard, J.-M. Designs for high-efficiency electrically pumped photonic nanowire single-photon sources. *Optics. Ex.* **18**, 21204 (2010).
 - ²⁶ Somaschi, N. *et al.* Near-optimal single-photon sources in the solid state. *Nat. Photon.* **10**, doi:10.1038/nphoton.2016.23 (2016).
 - ²⁷ Danckwerts, J., Ahn, K. J., Förstner, J. & Knorr, A. Theory of ultrafast nonlinear optics of Coulomb-coupled semiconductor quantum dots: Rabi oscillations and pump-probe spectra. *Phys. Rev. B* **73**, 165318 (2006).
 - ²⁸ Specht, J. F., Knorr, A. & Richter, M. Two-dimensional spectroscopy: An approach to distinguish Förster and Dexter transfer processes in coupled nanostructures. *Phys. Rev. B* **91**, 155313 (2015).
 - ²⁹ Scholes, G. D., Fleming, G. R., Olaya-Castro, A. & van Grondelle, R. Lessons from nature about solar light harvesting. *Nat. Chem.* **3**, 763–774 (2011).
 - ³⁰ Tahara, H., Ogawa, Y., Minami, F., Akahane, K. & Sasaki, M. Generation of undamped exciton-biexciton beats in InAs quantum dots using six-wave mixing. *Phys. Rev. B* **89**, 195306 (2014).
 - ³¹ Minkov, M. & Savona, V. Radiative coupling of quantum dots in photonic crystal structures. *Phys. Rev. B* **87**, 125306 (2013).
 - ³² Voss, T. *et al.* Biexcitonic effects in the coherent control of the excitonic polarization detected in six-wave-mixing signals. *Phys. Rev. B* **66**, 155301 (2002).
 - ³³ Tahara, H., Ogawa, Y., Minami, F., Akahane, K. & Sasaki, M. Long-time correlation in non-markovian dephasing of an exciton-phonon system in InAs quantum dot. *Phys. Rev. Lett.* **112**, 147404 (2014).
 - ³⁴ Gammon, D. *et al.* Nuclear spectroscopy in single quantum dots: Nanoscopic Raman scattering and nuclear magnetic resonance. *Science* **277**, 85 (1997).
 - ³⁵ Hameau, S., Guldner, Y., Verzele, O., Ferreira, R. & Bastard, G. Strong electron-phonon coupling regime in quantum dots: Evidence for everlasting resonant polarons. *Phys. Rev. Lett.* **83**, 4152 (1999).
 - ³⁶ Zibik, E. A. *et al.* Intraband relaxation via polaron decay in InAs self-assembled quantum dots. *Phys. Rev. B* **70**, 161305(R) (2004).
 - ³⁷ Yeo, I. *et al.* Strain-mediated coupling in a quantum dot-mechanical oscillator hybrid system. *Nat. Nanotech.* **9**, 106–110 (2014).

SUPPLEMENTARY MATERIAL

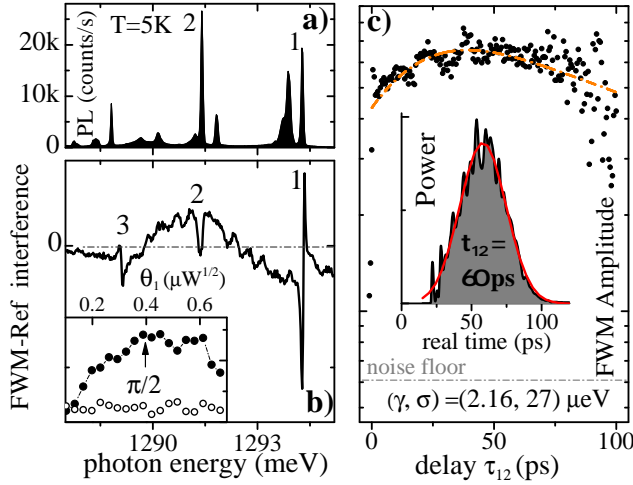
A. Sample fabrication.

The suspended PTs shown in Fig. 1 a, specifically developed for this work, offer improved mechanical stability and robustness with respect to stand-alone ones¹⁵. They were fabricated from a planar GaAs sample containing a single layer of InAs QDs grown by molecular beam epitaxy. After deposition of a hard mask by e-beam lithography, metal deposition and lift-off, the structures are defined by deep plasma etching with a controlled under etching angle of 4°. The PTs investigated in the main manuscript (Sample A) feature a length of 20 μm and a top diameter of 2.8 μm . Around the QDs, the waveguide section features a 0.25 μm diameter. Auxiliary pillars (used to reflect the reference field, \mathcal{E}_r) and PTs are respectively shifted by 15 μm , and are organized in pattern of five-by-five PTs, with a gradually varying PT top-diameters from 2 μm to 4 μm . By performing photo-luminescence (not shown, acquired under pulsed, non-resonant excitation) on the PT considered in the main manuscript, we observe that the QD saturation is achieved for a pump intensity as low as 0.4 μW . The transitions then feature a bright emission, with spectrally-integrated count rate of 400 kHz.

B. Coherence and FWM dynamics of InAs QDs in PTs: analysis of dephasing mechanisms. Supplementary examples.

PTs enable to retrieve FWM from single InAs QDs within a broad spectral range from 915 nm to 960 nm. To exemplify this broad-band operation, in Fig. S5 we

present results obtained on the sample (Sample B) containing QDs emitting at 960 nm, with respect to the one considered in the main manuscript (Sample A) emitting around 930 nm. In the Sample B, PTs have a length of $30\text{ }\mu\text{m}$, a top diameter of $4.5\text{ }\mu\text{m}$ and a taper angle of $\sim 8^\circ$, and thus are bigger than in the Sample A.



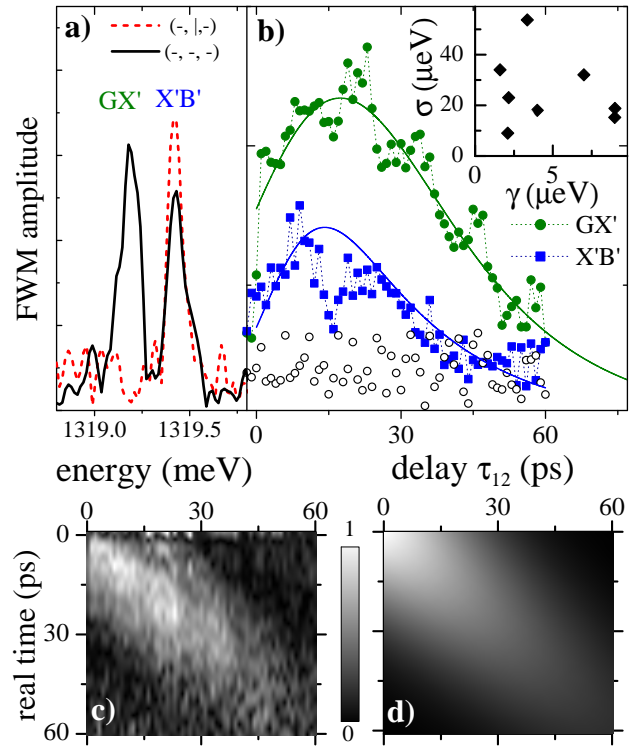
Supplementary Figure S5. **PL and FWM spectroscopy of InAs QDs emitting at 960 nm embedded in a photonic trumpet. Sample B.**

In Fig. S5 a we show a photoluminescence spectrum, non-resonantly excited at 1.4 eV with intensity of 30 nW, an order of magnitude below the QD saturation. A spectral interference at the FWM heterodyne frequency $2\Omega_2 - \Omega_1$, obtained on the same PT is shown in Fig. S5 b. Three, spectrally sharp features, correspond to the FWM from three individual transitions in InAs QDs. It is worth to note that the PL and FWM spectra are not the same. Transitions marked as “1” and “2” are observed in both experiments. Conversely, “3”, detected in FWM, does not have its counterpart in the PL. FWM amplitude of the transition “1” as a function of \mathcal{E}_1 pulse area θ_1 is shown in the inset. FWM reaches its maximum, corresponding to the $\theta_1 = \pi/2$ area, for \mathcal{E}_1 intensity of only $0.2\text{ }\mu\text{W}$, indicating an excellent coupling between the $\mathcal{E}_{1,2,3}$ driving fields and the exciton transition. Further increase of θ_1 results in the Rabi flopping and decrease of the FWM amplitude.

In order to infer dephasing mechanisms, we have first examined the time-resolved FWM for fixed $\tau_{12} = 60\text{ ps}$, displayed as an inset in Fig. S5 c. The response clearly reveals a Gaussian photon echo (the red trace corresponds to a Gaussian fit), with the temporal FWHM spread of $t_{\text{inh}} = 56\text{ ps}$ for the FWM amplitude. Such an echo in the FWM transient is a fingerprint of the spectral inhomogeneous broadening σ . Applying the model presented in Ref. [20], it is evaluated as $\sigma = \hbar\sqrt{8\ln 2}/t_{\text{inh}} = 27\text{ }\mu\text{eV}$. On a single exciton level, σ is attributed to the spectral wandering, occurring within the integration time²⁰. By varying the latter from 1 ms to 1 s we observe virtually the same echo behavior. We thus conclude that the spectral fluctuations of this transition occur at the

sub-ms timescale. Spectral positions of the transition “1” fluctuate with a characteristic spread of σ over the measurement. Despite their temporal separation, they all interfere with the reference field \mathcal{E}_r and give rise to the involved spectral shape of the resulting time-averaged interferogram. After applying Fourier-transform in the spectral interferometry algorithm, this yields a Gaussian response in time centered at $t = \tau_{12}$, i.e. photon echo. We note that excitons in all investigated PTs (statistics of γ and σ is shown in the inset of Fig. S6 b) displayed a measurable echo in their coherence dynamics, yielding σ up to $50\text{ }\mu\text{eV}$.

To assess the coherence dynamics, we have measured τ_{12} delay dependence of the FWM amplitude, displayed in Fig. S5 c. Suppression of the FWM for negative delays indicates lack of two-particle, biexcitonic state. We thus attribute the investigated transition “1” to a charged exciton. In the FWM delay dynamics, we observe initial rise, which is due to the echo formation, followed by an exponential decay. To simulate coherence evolution (depicted with the orange dashed line, also see Fig. 2 a and Fig. S6 b) of such inhomogeneously broadened transition, we implement the model presented in Ref. [20]. Bearing in mind previously determined σ , we retrieve the dephasing time $T_2 = (610 \pm 20)\text{ ps}$ as the only fitting parameter, corresponding to the homogeneous broadening of $\gamma = (2.16 \pm 0.07)\text{ }\mu\text{eV}$.



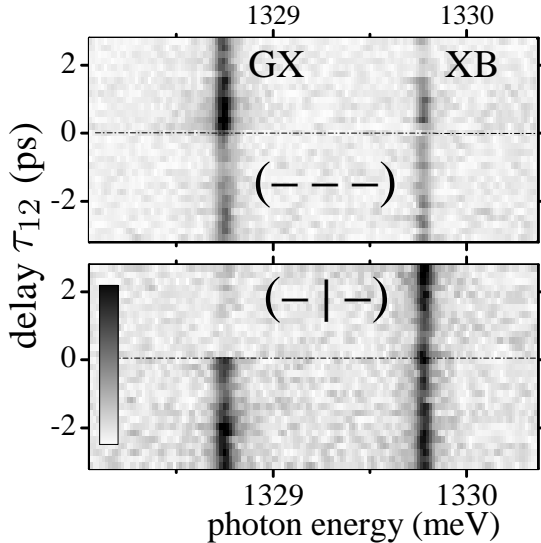
Supplementary Figure S6. **Coherence and FWM dynamics measured on an exciton-biexciton system showing an increased inhomogeneous broadening σ with respect to Fig. 2 and Fig. S5.**

In Fig. S6 a we present FWM spectra in $(\mathcal{E}_1, \mathcal{E}_2, \mathcal{E}_r) = (-, -, -)$ (black solid) and $(-, |, -)$ (red dashed) configuration on another PT in the Sample A, having a top-diameter of $2.9\text{ }\mu\text{m}$. Using

the FWM polarization selection rules (see Fig.S7), a pair of transitions (GX' , $X'B'$) is identified as an exciton-biexciton system, with a renormalization energy of $\Delta' = -0.24$ meV. The retrieved coherence dynamics is shown in Fig.S6 b, yielding in this case, $(\gamma_{GX'}, \sigma_{GX'}) = (7, 33) \mu\text{eV}$ and $(\gamma_{X'B'}, \sigma_{X'B'}) = (7, 58) \mu\text{eV}$. Clearly, larger σ deteriorates the coherence of both transitions, resulting in larger γ with respect to the example investigated in the main manuscript (Fig. 2). Note, a larger inhomogeneous broadening of $X'B'$ with respect to the GX' , indicating anti-correlation in spectral wandering of the exciton and the biexciton level. In the coherence dynamics we also identify exciton-biexciton beating with a period of $|2\pi\hbar/\Delta'| = 17$ ps. The noise floor is given by open circles.

The time-resolved FWM amplitude of the GX' as a function of τ_{12} is shown in Fig.S6 c. Due to a large σ (and thus sufficiently narrow width of the echo in time) such a map explicitly shows formation of the photon echo²⁰. Namely, we see the shift of the FWM maximum in real time t according to τ_{12} , forming a Gaussian centered along the diagonal line $\tau_{12} = t$, as reproduced by the simulation shown in Fig.S6 d.

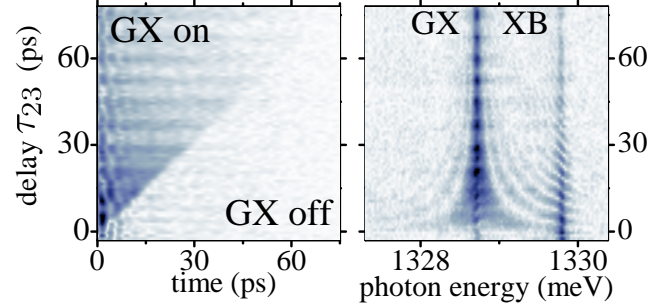
C. Identification of the exciton-biexciton system via FWM selection rules



Supplementary Figure S7. **Identification of GX and XB as a ground state-exciton and exciton-biexciton transition in a single InAs QD.** Delay dependence of the FWM for $-3.2 \text{ ps} < \tau_{12} < 2.8 \text{ ps}$, for co-linearly polarized \mathcal{E}_1 , \mathcal{E}_2 and the reference $(-, -, -)$ (top) and for cross-polarized \mathcal{E}_2 ; $(-, |, -)$ (bottom). Detection along $(-)$ direction.

The resonances discussed in the main manuscript at 1328.74 meV and 1329.8 meV are recognized as ground state - exciton (GX) and exciton - biexciton (XB) transitions. We apply the FWM polarization and delay selection rules presented in Ref. [20]. In Fig. S7, we show FWM amplitude of GX and XB, as a function of τ_{12} , around zero delay for co- and cross-linearly polarized \mathcal{E}_1 and \mathcal{E}_2 , for $(\theta_1, \theta_2) = (\pi/5, 2\pi/5)$. For negative delays, the FWM is the same for both polarization configurations: \mathcal{E}_2 arrives first and induces a two-photon coherence (TPC) between G and B. \mathcal{E}_1 converts TPC into the FWM released with equal amplitudes on GX and XB. Conversely, for positive delays the FWM can be generated in two manners. For co-linearly polarized \mathcal{E}_1 and \mathcal{E}_2 the FWM is created via density grating, with the amplitude twice larger at GX than at XB (in the χ^3 , perturbative regime). Instead, for cross-polarized excitation, the signal is created via Raman coherence between GX and GY, such that the signal is released uniquely at XB. Finally, we note that we also measured the fine-structure beating with a period of 50 ps, yielding the splitting between GX and GY of $\delta = 83 \mu\text{eV}$ (not shown).

D. Temporal gating and engineering of the FWM spectral lineshape via FWM/SWM switching



Supplementary Figure S8. **Coherent control of the FWM signal of the exciton-biexciton system in QD1 (Sample A), via FWM/SWM switching mechanism.**

FWM amplitude of the GX transition in QD1, discussed in the main manuscript, as a function of the real time and delay τ_{23} of the control pulse \mathcal{E}_3 is shown in the left panel in Fig. S8. FWM is present uniquely prior to the arrival of \mathcal{E}_3 , showing temporal gating of the signal. Linear color scale. In the right panel we show FWM spectral amplitudes. Owing to an abrupt suppression of the FWM in the real time, a considerable spectral broadening and sidebands for both GX and XB are observed for initial delays τ_{23} , followed by a gradual recovery of the Lorentzian lineshapes with increasing τ_{23} .